Impact of Permittivity Patterns on Fully Polarimetric Brightness Temperature Signatures at L-band

Link, Moritz; Montzka, Carsten; Jagdhuber, Thomas; Søbjærg, Sten S.; Dill, Stephan; Peichl, Markus; Meyer, Thomas; Jonard, François

Published in:
Electromagnetic Waves (Progress in electromagnetics research)

Publication date:
2019

Document Version
Publisher's PDF, also known as Version of record

Progress In Electromagnetics Research, Vol. 166, 75–93, 2019

Impact of Permittivity Patterns on Fully Polarimetric Brightness Temperature Signatures at L-Band

Moritz Link[1, *], Carsten Montzka[2], Thomas Jagdhuber[1], Sten S. Søbjærg[3], Stephan Dill[1], Markus Peichl[1], Thomas Meyer[2], and François Jonard[2, 4]

Abstract—This study investigates the sensitivity of L-band (1.41 GHz) polarimetric brightness temperature signatures to oriented permittivity patterns, which can occur for example in the case of row and interrow soil moisture differences in agricultural fields. A field experiment and model simulations are conducted to verify the effects of such patterns on all four Stokes parameters. We find that for an artificial target resembling idealized model conditions, permittivity patterns lead to systematic brightness temperature modulations in dependency of the azimuthal look angle. For the specific field setup, modulations reach amplitudes of ~ 4 K and mostly affect h-polarized brightness temperatures as well as the first, second, and third Stokes parameters. Simulations of soil moisture patterns under idealized model conditions indicate even higher amplitudes (up to 60 K for extreme cases). However, the effects occur only for permittivity layer widths of up to 8 cm (given the observing wavelength of 21 cm), which is lower than the row and interrow widths typically observed in agricultural settings. For this reason, and due to the idealized model geometry investigated here, future studies are needed to transfer the findings of this study to potential applications such as the sensing of oriented soil moisture patterns. Particular interest might lie in radiometry and reflectometry in lower frequency ranges such as P-band, where according to the threshold established here (8/21 wavelengths), permittivity layer widths of up to ~ 45 cm could be observed.

1. INTRODUCTION

The Earth's thermal microwave emission at L-band (1–2 GHz) contains information on key elements of the terrestrial water cycle such as surface soil moisture, commonly defined as the water content of the first few centimeters of the soil [1, 2]. Two satellite missions dedicated to soil moisture monitoring currently make use of radiometric observations at L-band (1.41 GHz): The Soil Moisture and Ocean Salinity (SMOS) mission of the European Space Agency (ESA), launched in 2009, [3] and the Soil Moisture Active and Passive (SMAP) mission of the National Aeronautics and Space Administration (NASA), launched in 2015 [4]. Further applications of L-band radiometric observations include the estimation of sea surface salinity [5], soil freeze/thaw conditions [6] as well as characterizations of sea ice, polar ice cover and permafrost [7–9].

Retrieval algorithms of geophysical variables typically make use of microwave brightness temperature (Tb) measurements in horizontal (Tb_h) and vertical (Tb_v) polarization. However, fully polarimetric radiometers like SMOS and SMAP are able to measure the full polarization state of the incoming wave, which can be described by the four elements of the Stokes vector: The sum of Tb_v and Tb_h (I), difference between Tb_v and Tb_h (Q), difference between 45-degree and -45-degree linear

Received 2 August 2019, Accepted 19 October 2019, Scheduled 20 November 2019
* Corresponding author: Moritz Link (moritzlink0@gmail.com).
[1] German Aerospace Center (DLR), Microwaves and Radar Institute, PO BOX 1116, Wessling 82234, Germany. [2] Forschungszentrum Jülich GmbH, Institute of Bio- and Geosciences: Agrosphere (IBG-3), Jülich 52425, Germany. [3] National Space Institute, Technical University of Denmark, Kongens Lyngby 2800, Denmark. [4] Université catholique de Louvain, Earth and Life Institute, Louvain-la-Neuve 1348, Belgium.

polarized Tb (U) as well as difference between left-hand and right-hand circular polarized Tb (V). U and V correspond to the real and imaginary part of the complex correlation between Tb_h and Tb_v, respectively [10]. The additional information content in these parameters might be used during retrievals of environmental variables or to derive new knowledge about the observed target.

It is understood that fully polarimetric brightness temperature observations are sensitive to azimuthal asymmetry, e.g., in the case of oriented non-spherical particles [11, 12] or periodic surface roughness conditions such as ocean waves [13, 14]. In addition, agricultural fields have shown azimuth-angle dependent brightness temperature signatures in ground-based [15–18], airborne [19] and satellite [20] observations. Such effects were observed over both bare soil and grown plants [15], which was attributed to tillage-induced periodic soil roughness conditions [21, 22] and plant row alignment [23], respectively. However, previous studies indicate that in agricultural fields, azimuthal anisotropy also exists with respect to soil moisture patterns. Specifically, systematic soil moisture differences in the row and interrow position have been observed by various authors over corn [24–29] and soybean [30] fields, which was attributed to, amongst others, localized irrigation [28, 29], stem flow [28–30] and differences in root water uptake and infiltration [24, 30, 31]. Observed row-interrow soil moisture differences reach up to $\sim$ 10 vol.% [28, 30] (even higher for localized irrigation [29]) and have been reported for large parts of the growing season [25, 30] as well as both tillage and no-tillage conditions [25, 26, 29]. Such row and interrow soil moisture variations effectively result in conditions of anisotropic soil permittivity. Previous studies suggest that these permittivity conditions can lead to azimuthal variations of all four Stokes parameters [32]. This could introduce uncertainties in soil moisture retrievals as well as open up opportunities for detecting soil moisture patterns; however, such effects have not yet been assessed at low frequencies such as L-band. In addition, theory suggests that strong constraints on the permittivity layer widths exist [32–35], such that it remains an open question if moisture patterns in agricultural fields (row spacings of $\sim$ 20–80 cm) can lead to observable effects at L-band (wavelength $\sim$ 20 cm).

The objectives of this study are to (i) assess the effects of oriented permittivity patterns on polarimetric brightness temperature observations at L-band and (ii) investigate the largest permittivity layer widths causing such effects. A controlled field experiment with an artificial measurement target was conducted, including permittivity layer widths of 2, 4, 8, 16 and 32 cm. Observations from the field experiment were compared to simulations of a fully polarimetric emission model [32]. Based on the findings, the relevance of soil moisture patterns for radiometric observations at L-band and other frequency ranges is discussed. We describe the fully polarimetric emission model in Section 2, depict the field experiment setup in Section 3, outline the specific simulation methodology regarding the field experiment in Section 4, present the results in Section 5, discuss the findings and their relevance to real-world scenarios in Section 6 and conclude the study in Section 7.

2. POLARIMETRIC MICROWAVE EMISSION OF A SMOOTH SURFACE WITH ORIENTED PERMITTIVITY PATTERN

The polarization state of a partially polarized electromagnetic wave is fully described by the four parameters of the Stokes vector $\overline{Tb}$ [10]:

$$\overline{Tb} = \begin{bmatrix} I \\ Q \\ U \\ V \end{bmatrix} = \begin{bmatrix} Tb_v + Tb_h \\ Tb_v - Tb_h \\ Tb_{45} - Tb_{-45} \\ Tb_{lc} - Tb_{rc} \end{bmatrix} = \frac{\lambda^2}{kz} \begin{bmatrix} \langle E_v^2 \rangle + \langle E_h^2 \rangle \\ \langle E_v^2 \rangle - \langle E_h^2 \rangle \\ \mathrm{Re}\langle E_v E_h^* \rangle \\ \mathrm{Im}\langle E_v E_h^* \rangle \end{bmatrix} \tag{1}$$

with Tb_{45}, Tb_{-45}, Tb_{lc} and Tb_{rc} denoting the brightness temperature of 45°, −45°, left-hand circular and right-hand circular polarization, respectively. E_v and E_h are the vertical and horizontal electric field components, respectively, whereas $\langle \bullet \rangle$ indicates averaging in time and $*$ denotes complex conjugation. λ, k and z denote the wavelength, Boltzmann's constant and the impedance of the medium, respectively.

[32] describes analytical formulations for the fully polarimetric emission of a smooth surface with an anisotropic (oriented) permittivity pattern. The key formulations are revisited in the following, since [32] is available in German only. The model considers a smooth infinite half-space with periodically striped layers of widths d_1 and d_2 of complex permittivites ε_1 and ε_2, respectively. A schematic depiction of the model geometry is provided in Figure 1(a). As general condition, the model requires the permittivity

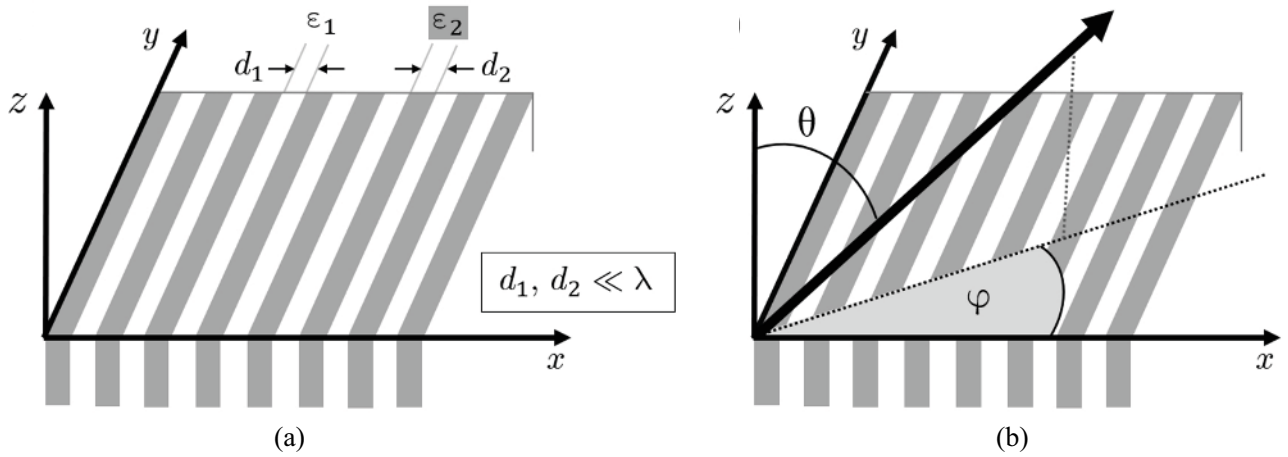

Figure 1. (a) Model geometry of a smooth half space with alternating parallel dielectric layers of permittivities ε_1, ε_1 and widths d_1, d_2. (b) Angular convention for incidence (θ) and azimuth (ϕ) angles used in this paper. Figure adapted from [32, Figures 3.9 and 3.11].

layer widths to be significantly smaller than the observing wavelength ($d_1, d_2 \ll \lambda$). This threshold ensures that the half-space acts as form-birefringent uniaxial crystal, whose anisotropic permittivity can be expressed through a dyadic tensor [32, 34]:

$$\underline{\varepsilon} = \begin{bmatrix} \varepsilon_x & 0 & 0 \\ 0 & \varepsilon_y & 0 \\ 0 & 0 & \varepsilon_y \end{bmatrix}, \tag{2}$$

where ε_x and ε_y are effective permittivities of the medium in the x and y direction, respectively, given by [32–34]:

$$\varepsilon_x = \frac{(d_1 + d_2) \cdot \varepsilon_1 \cdot \varepsilon_2}{\varepsilon_1 \cdot d_1 + \varepsilon_2 \cdot d_2}, \quad \varepsilon_y = \frac{d_1 \cdot \varepsilon_1 + d_2 \cdot \varepsilon_2}{d_1 + d_2}. \tag{3}$$

Note that under the assumption of equal layer widths, d_1 and d_2 can be replaced with unity ($d_1 = d_2 = 1$). When a plane wave irradiates on the medium under incidence angle θ and azimuth angle ϕ (see Figure 1(b) for angular convention), the direction of propagation for the incident, scattered and transmitted wave ($\vec{k}_i$, $\vec{k}_r$, and $\vec{k}_t$) are given by [32]:

$$\vec{k}_i = k_0 \cdot \begin{bmatrix} \sin\theta \cdot \cos\phi \\ \sin\theta \cdot \sin\phi \\ -\cos\theta \end{bmatrix}, \quad \vec{k}_r = k_0 \cdot \begin{bmatrix} \sin\theta \cdot \cos\phi \\ \sin\theta \cdot \sin\phi \\ \cos\theta \end{bmatrix}, \quad \vec{k}_t = k_0 \cdot \begin{bmatrix} \sin\theta \cdot \cos\phi \\ \sin\theta \cdot \sin\phi \\ -\sqrt{n^2 - \sin^2\theta} \end{bmatrix}, \tag{4}$$

with $k_0 = 2\pi/\lambda$ denoting the wavenumber in free space, n denoting the complex refractive index of the medium and the first, second and third vector elements correspond to the x-, y-, and z-directions of Figure 1, respectively. For the anisotropic medium described above, two solutions exist for n, namely an ordinary refraction index n_o and an extraordinary refractive index n_{eo} [32]:

$$n_o = \sqrt{\varepsilon_y}, \quad n_{eo} = \sqrt{\varepsilon_x + \sin^2\theta \cdot \cos^2\phi \cdot \frac{\varepsilon_y - \varepsilon_x}{\varepsilon_y}}. \tag{5}$$

Following Eqs. (4) and (5), two possible propagation directions of the transmitted wave exist in the z-direction: an ordinary and an extraordinary direction. For these cases, the electric field vectors are given by [32]:

$$\vec{E}_{to} = \frac{E_{to}}{\sqrt{n_o^2 - \sin^2\theta \cdot \cos^2\phi}} \cdot \begin{bmatrix} 0 \\ \sqrt{n_o^2 - \sin^2\theta} \\ \sin\theta \cdot \sin\phi \end{bmatrix}, \quad \vec{E}_{teo} = E_{teo} \cdot \begin{bmatrix} \alpha_x \cdot \sin\theta \cdot \cos\phi \\ \alpha_y \cdot \sin\theta \cdot \sin\phi \\ \alpha_y \cdot \sqrt{n_{eo}^2 - \sin^2\theta} \end{bmatrix}, \tag{6}$$

where $\vec{E}_{to}$, $\vec{E}_{teo}$ are the electric field vectors of the ordinary and extraordinary directions, respectively; E_{to}, E_{teo} are the respective electric field amplitudes and α_x, α_y are given by [32]:

$$\alpha_m = \frac{\alpha'_m}{\sqrt{\alpha'^2_x \cdot \sin^2\theta \cdot \cos^2\phi + \alpha'^2_y \cdot (n^2_{eo} - sin^2\theta \cdot sin^2\phi)}}, \quad \alpha'_m = \frac{1}{n^2_{eo} - \varepsilon_m}, \quad m = x, y. \tag{7}$$

From Eqs. (6) and (7), the following four equations arise for the reflected and transmitted electrical field amplitudes [32]:

$$\underline{M} \cdot \begin{bmatrix} E_{rh} \\ E_{rv} \\ E_{to} \\ E_{teo} \end{bmatrix} = \begin{bmatrix} -\sin\phi \cdot E_{ih} + \cos\theta \cdot \cos\phi \cdot E_{iv} \\ \cos\phi \cdot E_{ih} + \cos\theta \cdot \sin\phi \cdot E_{iv} \\ \cos\theta \cdot \cos\phi \cdot E_{ih} + \sin\phi \cdot E_{iv} \\ \cos\theta \cdot \sin\phi \cdot E_{ih} - \cos\phi \cdot E_{iv} \end{bmatrix}, \tag{8}$$

where E_{rh}, E_{rv} are the reflected, and E_{ih}, E_{iv} are the incident electric field amplitudes of horizontal and vertical polarization, respectively, and $\underline{M}$ is a 4×4 transformation matrix given in Appendix A. From Eq. (8) it is possible to derive analytical formulations for the scattering amplitudes f_{hh}, f_{hv}, f_{vh} and f_{vv}, which relate the incident and reflected electrical field amplitudes as [32]:

$$\begin{bmatrix} E_{rh} \\ E_{rv} \end{bmatrix} = \begin{bmatrix} f_{hh} & f_{hv} \\ f_{vh} & f_{vv} \end{bmatrix} \cdot \begin{bmatrix} E_{ih} \\ E_{iv} \end{bmatrix}. \tag{9}$$

The formulations for f_{hh}, f_{hv}, f_{vh}, and f_{vv} are provided in Appendix B. Note that the scattering amplitudes correspond to purely specular reflection. Consequently, the bistatic scattering coefficient of the medium can be derived as [32]:

$$\gamma_{pq}(\theta_s, \phi_s; \theta, \phi) = |f_{pq}(\theta, \phi)|^2 \cdot 4\pi \cdot \delta(\cos\theta_s - \cos\theta) \cdot \delta(\phi_s - \phi), \tag{10}$$

where $\gamma_{pq}(\theta_s, \phi_s; \theta, \phi)$ is the bistatic scattering coefficient of incidence and scattering polarizations p and q, incidence and scattering off-nadir angles θ and θ_s as well as incidence and scattering azimuth angles ϕ and ϕ_s, respectively. $\delta(\cdot)$ denotes the delta function. From Eqs. (9) and (10) it can be shown that the Stokes vector takes the following form [32]:

$$\overline{Tb} = \begin{bmatrix} I \\ Q \\ U \\ V \end{bmatrix} = T \cdot \begin{bmatrix} 2 - |f_{hh}|^2 - |f_{vh}|^2 - |f_{hv}|^2 - |f_{vv}|^2 \\ |f_{hh}|^2 + |f_{vh}|^2 - |f_{hv}|^2 - |f_{vv}|^2 \\ 2 \cdot \mathrm{Re}(f_{hh} \cdot f^*_{hv} + f_{vh} \cdot f^*_{vv}) \\ 2 \cdot \mathrm{Im}(f_{hh} \cdot f^*_{hv} + f_{vh} \cdot f^*_{vv}) \end{bmatrix}, \tag{11}$$

where T is the physical temperature of the medium.

Based on the above formulations, which have been directly revisited from [32], the polarimetric emission of a smooth surface with oriented permittivity layers is expected to vary with azimuth angle (ϕ), incidence angle (θ), permittivities (ε_1, ε_2) as well as the ratio of permittivity layer widths (ratio of d_1 and d_2). Note that all formulations are frequency-independent; however, they are valid only for permittivity layer widths significantly smaller than the wavelength of observation ($d_1, d_2 \ll \lambda$). The exact break point of this threshold is not well understood. [35] simulate polarization conversion by means of dielectric form birefringence and utilize layer thicknesses of $d_1, d_2 = \lambda/4$, noting that the model is likely valid while $d_1, d_2 < \lambda/2$. [33] notes that the threshold likely depends on polarization and propagation direction. We investigate this threshold for L-band at 1.41 GHz, an incidence angle of 40°, azimuth angles of 0–360° and all four Stokes parameters by means of a controlled field experiment (see Section 3).

3. FIELD EXPERIMENT

A field experiment was conducted to assess polarimetric brightness temperature signatures of anisotropic permittivity patterns at L-band. We describe the test site setup in Section 3.1, the measurement target in Section 3.2 and the radiometer system in Section 3.3.

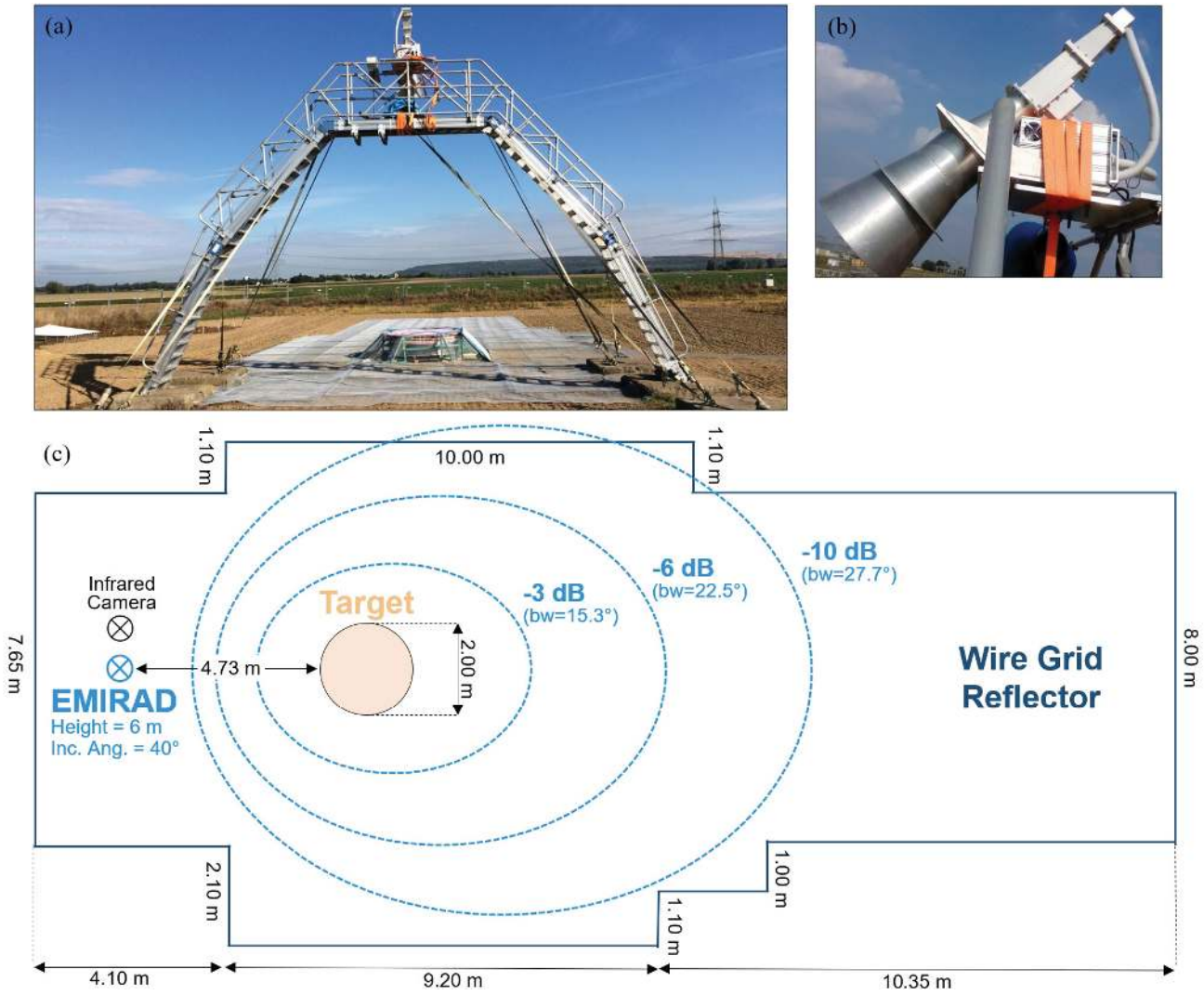

Figure 2. (a) Picture of the measurement setup at the remote sensing field laboratory of FZ Jülich. (b) EMIRAD radiometer mounted on top of the aluminum arc. (c) Top-view sketch (not to scale) showing the locations of the EMIRAD radiometer, infrared camera, rotating target and wire grid. Note that the wire grid setup was not exactly rectangular. Dashed lines indicate the radiometer footprints at -3 dB, -6 dB, and -10 dB and their beamwidths (adapted from [36, Figure 1]).

3.1. Test Site

The experiment was conducted at the Forschungzentrum Jülich remote sensing field laboratory in Selhausen, Germany, between the 4th and 13th of September 2017. Pictures and a sketch of the experimental setup are shown in Figure 2, whereas further information on the Selhausen remote sensing field laboratory can be found in [36]. The EMIRAD L-band radiometer [37] was installed at about 6 m height on an aluminum arc and directed towards the target (2 m in diameter and 0.75 m in height) at an incidence angle of 40°. Microwave emission from the surrounding area was hereby shielded by a wire mesh grid on the ground (see Figures 2(a) and 2(c)) with a mesh size of ≤ 1 cm, acting as an almost ideal reflector at L-band [36, 38]. Emission from the support structure of the target was shielded by the same wire mesh material (see Figures 2(a) and 3(b)). There was also an infrared camera installed on the arc next to the radiometer, which was used to carry out complementary temperature measurements of the target surface in addition to in situ probing with digital thermometer measurements.

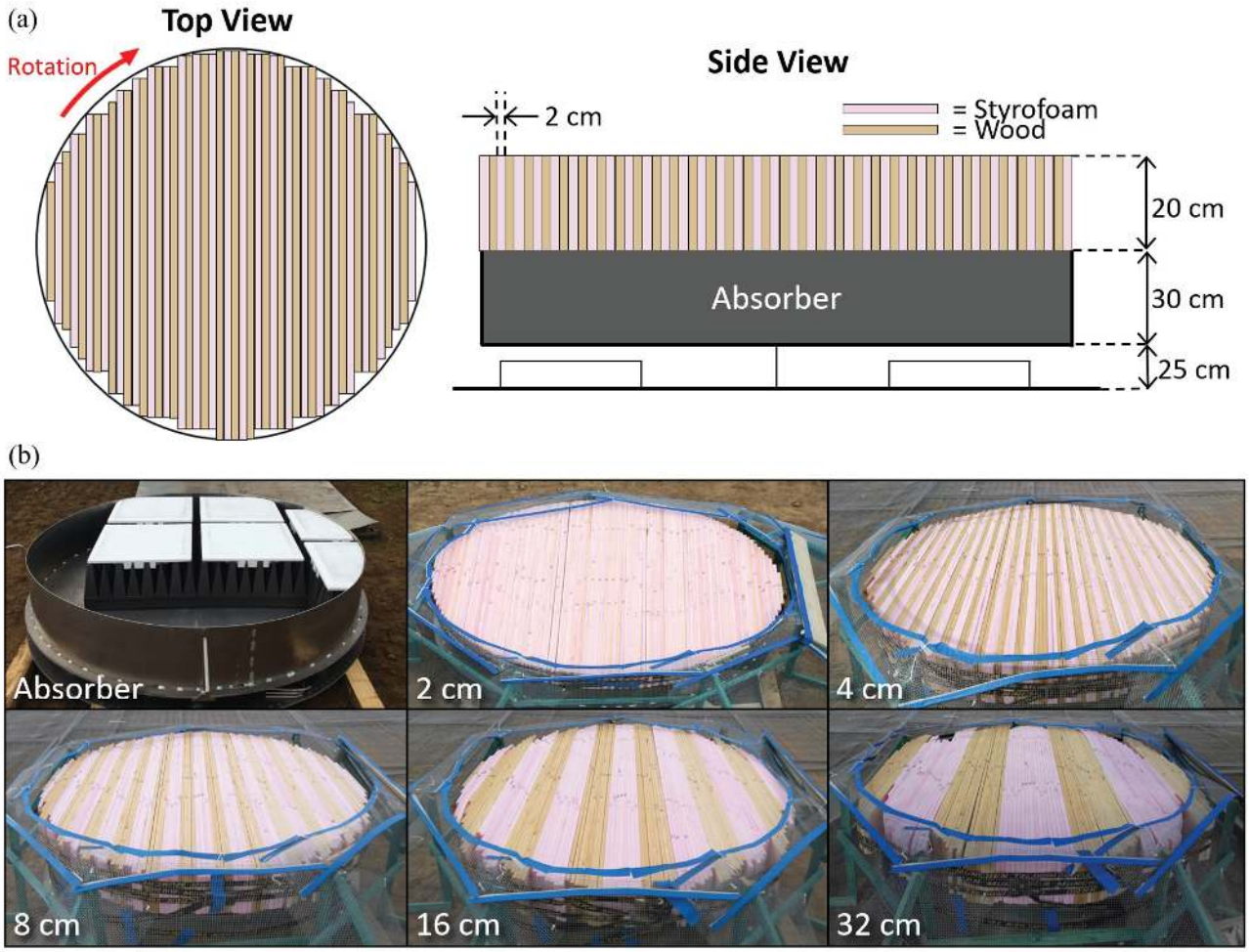

Figure 3. (a) Sketch of the rotating target from a top and side view. (b) Assembly of the pyramidal absorber material within the metallic rotating measurement box (partly filled at time of photograph) as well as different target configurations with varying layer widths (2, 4, 8, 16 and 32 cm).

3.2. Measurement Target

To ensure controlled experiment conditions and to assess various permittivity layer widths, an artificial measurement target was used in this study. The target was constructed from alternating layers of spruce wood and Styrofoam, representing anisotropic permittivity conditions as depicted in Figure 1. The two materials are characterized by substantial permittivity differences at L-band (see Table 1), with Styrofoam being close to the permittivity of air. The alternating layering was achieved by assembling wood and Styrofoam planks in a circular structure as depicted in Figure 3(a). By re-arranging the planks inside the circular structure, layer widths of 2, 4, 8, 16 and 32 cm could be achieved as depicted in Figure 3(b). The target height was hereby constant at 20 cm for all arrangements. Note that we expect the model assumptions to hold only for layer widths of 2, 4 and 8 cm ($d_1, d_2 < \lambda/2$, see discussions in Section 2). However, to verify the break point of this threshold, we have also conducted measurements for larger layer widths (16 and 32 cm). To achieve measurements from different azimuthal view angles, the target was placed on a rotating stainless metal support structure (Figure 3(a)) supported by a ring mount bearing. Between the support structure and the target, a layer of microwave absorbers was placed to avoid reflections from the metal surface. The absorber material had a thickness of 30 cm, being characterized by a return loss of < 30 dB at 1.4 GHz. Figure 3(b) shows the rotating measurement box partly filled with the pyramidal absorber and endcaps on the tips. In the above-described configuration, brightness temperature observations were conducted for 360° target rotations in 15° increments. The

total measurement time for a 360° rotation was roughly 90 minutes.

3.3. EMIRAD Radiometer

EMIRAD is a fully polarimetric L-band (1.41 GHz) radiometer of the correlation type [37], hence it yields parallel measurements of the full Stokes vector. Figure 2(b) shows the radiometer in its measurement position during the field experiment. A Potter horn antenna with 50 cm aperture was used, leading to a −3 dB half-power beam width of 15.3°. Since the footprint of the antenna was significantly larger than the target area (see Figure 2(c)), background radiance corrections were applied as described in Section 4.2. An integration time range of 30–100 s was hereby used for both observation and calibration measurements, leading to an estimated precision of < 0.2 K for all polarimetric observables. Internal calibration was based upon a matched load and an active cold load [39]. Cable losses between receiver and antenna were calibrated once per day using a liquid nitrogen cooled target, whereas cable phase variations remained stable within 1° (based on measurements prior to and after the campaign). Antenna system effects (phase difference, insertion loss, return loss, cross talk) were corrected in the data processing based on reference values for the EMIRAD radiometer, estimated using a high-end vector network analyzer and cold sky observations. The instrument was aligned horizontally with an estimated accuracy in the order of 1°, minimizing polarization mixing between the second and third Stokes parameters. Finally, the digital back-end of the radiometer features real-time radio frequency interference (RFI) detection through estimation of kurtosis, whereas no RFI contamination was recorded during the field experiment.

4. FIELD EXPERIMENT MODELING APPROACH

To simulate the signal received by the radiometer during the field experiment, we adapt a modeling approach after [36]. The total received p-polarized brightness temperature Tb^p is hereby expressed as a linear combination of target and background contributions [36]:

$$Tb^p = \eta \left[(1 - R_t^p)\, T_t + R_t^p Tb_{sky} \right] + (1 - \eta) \left[(1 - R_0^p)\, T_0 + R_0^p Tb_{sky} \right] \tag{12}$$

where η [-] is a weighting factor accounting for the fractions of brightness temperature contributions originating from the target and background; R_t^p [-] and R_0^p [-] are the p-polarized reflectivities of the target and background, respectively; T_t [K] and T_0 [K] are the physical temperatures of the target and background, respectively; and Tb_{sky} [K] is the downwelling sky brightness temperature. Note that a potential polarization-dependency of η is not expressed here for brevity. An overview of all utilized parameters is found in Table 1, whereas the derivation of these parameters is described in the following.

4.1. Target Radiance Term

The target radiance term, i.e., the left summand in Eq. (12), constitutes the brightness temperature contribution originated from the measurement target. To model the term, four variables (Tb_{sky}, T_t, η and R_t^p) are required that are described in the following.

The sky temperature is a constant source of microwave radiation that is reflected from the target surface. Constant conditions of $Tb_{sky} = 4.8$ K [36] were assumed during the campaign.

The target physical temperature T_t is necessary to model the thermal microwave emission of the target. T_t was assessed regularly (every $\sim$ 20–30 minutes) during the campaign by means of a hand-held digital thermometer that was inserted into the Styrofoam structure of the target. Observations of an infrared camera confirmed that the above-named technique provided good estimates of the average target surface temperature (generally within $\sim$ 1°C). We have identified two time intervals of similar target temperature conditions: During the first interval (5th and 7th of September 2017; corresponding to 2, 4 and 8 cm permittivity layers), the target showed relatively high temperatures of $\sim$ 19–27°C. During the second measurement campaign interval (11th and 12th of September 2017; corresponding to 16 and 32 cm permittivity layers), the target showed lower temperatures of $\sim$ 13–20°C. Since target temperature variations of less than 10°C lead to negligible brightness temperature variations in our simulations (not exceeding 0.1 K difference in azimuthal amplitudes), we have utilized the average

Table 1. Parameters for simulations of target and background radiance terms.

Parameter	Symbol	Value	Unit
Target permittivity (Styrofoam)	ε_s	$1.04 - 0i$	[-]
Target permittivity (Wood)	ε_w	$3.5(\pm 0.5) - 0.8(\pm 0.2)i$	[-]
Radiance weighting factor	η	$0.105(\pm 10\%)$	[-]
Target physical temperature	T_t	296.15^a, 289.65^b	[K]
Background radiance	$Tb^{b,p}$	28.5^c, 28.8^d	[K]
Sky temperature	Tb_{sky}	4.8	[K]

^{a}2, 4 and 8 cm layers ^{b}16 and 32 cm layers
^{c}H-polarization ^{d}V-polarization

values ($T_t = 296.15$ K for the first interval, $T_t = 289.65$ K for the second interval) as target temperature parametrization for the respective intervals.

The weighting factor η accounts for the fraction of brightness temperature contributions originating from the target. In this study, η was estimated after a measurement-based approach of [36]. Hereby, two brightness temperature measurements of the target and surrounding area were conducted. During the first measurement the target was covered by a reflector (a wire mesh grid overlaid by a copper sheet), such that the target reflectivity can be assumed to be approximately unity. During the second measurement the target was covered by an absorber, such that the target reflectivity can be assumed to be approximately zero. By inserting $R_t^p = 1$ for the first measurement and $R_t^p = 0$ for the second measurement, Eq. (12) becomes a system of two equations with two unknowns η and R_0^p (the temperature of the surrounding area T_0 was hereby assumed to equal the air temperature). Evaluating these equations yielded estimates of $\eta = 0.105$ for both h- and v-polarization. The same weighting factor was utilized for the third and fourth Stokes parameters. Note that [36] also adopted an approach to calculate η from the normalized antenna directivity, which was not attempted in this study. Both approaches led to similar results within a $\sim 10\%$ range, and we add the same uncertainty bound to our estimate of η.

Finally, the reflectance of the target is under assumption of thermal equilibrium given by $R_t^p = 1 - e_t^p$, where e_t^p represents the target emissivity. To model e_t^p based on the emission model described in Section 2 [32] and under the assumption of equal layer widths, the complex relative permittivities of the Styrofoam (ε_s) and wood material (ε_w) are the only two variables required. Based on laboratory measurements carried out at the Microwaves and Radar Institute of the German Aerospace Center (DLR), the permittivity of the Styrofoam planks was assessed to be $\varepsilon_s = 1.04 - 0i$ at 1.4 GHz. The permittivity of wood was parametrized based on a two-step procedure. As a first step, permittivity measurements of a spruce wood sample were carried out at DLR, utilizing the transmission/reflection method [40]. The wood sample had a known gravimetric moisture content of 12% and similar fiber characteristics with respect to the target wood planks. The measurements yielded complex permittivities of $\varepsilon_w = 2 - 0.25i$ (longitudinal-structured fiber) and $\varepsilon_w = 3.5 - 0.8i$ (cross-structured fiber) at 1.4 GHz. However, two aspects need to be taken into account: Firstly, for logistical reasons it was not possible to conduct permittivity measurements of the exact wood planks used during the campaign. Secondly, due to the relative humidity conditions during the campaign, the wood moisture content of the target was likely higher with respect to the wood sample available for permittivity measurements. Consequently, as a second step, the wood permittivity measurements obtained at DLR were corrected for the expectedly higher moisture content of the target wood. For typical air temperature conditions (20°C) and the high end of observed relative humidity conditions (75–90%) during the campaign, the equilibrium moisture content of spruce wood is expected to be in the range of $\sim$ 15–21% [41, 42]. Measurements obtained in [43, 44] suggest that for this moisture content range, the permittivity of spruce wood is expected to range between $\sim$ 2–4 (real part) and 0–1 (imaginary part). Since the spruce wood measured at DLR, structurally similar to the target wood, yielded slightly higher permittivity values (given the same moisture content of 12%) with respect to the results reported in [43, 44], we chose to carry forward the higher end of the ranges in [43, 44]. In addition, a considerable parameter uncertainty bound was retained to account for the anisotropic permittivity characteristics of wood [45] and uncertainties in

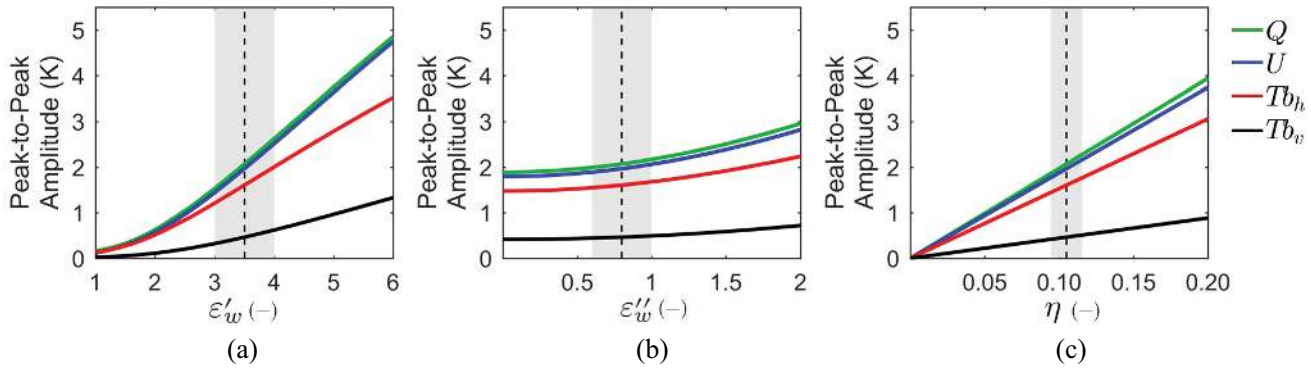

Figure 4. Sensitivity of brightness temperature azimuthal variations to (a) the real part of the wood permittivity ε'_w, (b) the imaginary part of the wood permittivity ε''_w and (c) the target radiance weighting factor η. Constant parameters of the sensitivity analysis are the same as in Table 1. Vertical dashed lines indicate the parameters utilized for forward simulations in this study with their respective uncertainty bounds shaded grey (see Table 1). The physical temperature is assumed to be 293 K.

the permittivity estimation process. Following this rationale, the wood parametrization utilized in this study is 3.5 ($\pm$0.5) (real part of permittivity) and 0.8 ($\pm$0.2) (imaginary part of permittivity).

4.2. Background Radiance Term

The background radiance term, i.e., the right summand in Eq. (12), can be considered an offset to the brightness temperature signatures received from the target. Since this study focuses on azimuthal brightness temperature variations that are not affected by this offset, no explicit background radiance modeling was conducted. Instead, we denoted the term with a single polarization-dependent variable $Tb^{b,p}$ that is assumed to stay approximately constant during the measurement campaign:

$$Tb^{b,p} = (1 - R_0^p)\, T_0 + R_0^p Tb^{sky} \tag{13}$$

where $Tb^{b,p}$ was estimated by conducting brightness temperature measurements of the target covered by a reflector, such that the target and surrounding area reflectivity can be assumed to be unity. Using this method, background radiance terms of $Tb^{b,h} = 28.5$ K and $Tb^{b,v} = 28.8$ K were derived. For the third and fourth Stokes parameters, any offsets from zero (i.e., offsets from a mean brightness temperature level of 0 K) are ignored in our analysis; consequently, we set the background radiance term to zero in these cases.

5. RESULTS

5.1. Sensitivity Analysis

To assess the influence of individual parameters as well as the effects of parameter uncertainty, Figure 4 investigates the sensitivity of simulated brightness temperature azimuthal variations to (a) the real part of the wood permittivity ε'_w, (b) the imaginary part of the wood permittivity ε''_w and (c) the target radiance weighting factor η. The investigated ε'_w and ε''_w ranges correspond to feasible wood permittivity values given realistic equilibrium moisture contents of 0–25% [43]. For clarity, we focus on amplitudes of Q, U, Tb_h and Tb_v (phases and periods of the azimuthal signatures are shown in Figures 5 and 6). It is evident from Figure 4 that azimuthal brightness temperature variations show a high sensitivity to ε'_w, with a steep and quasi-linear response after $\varepsilon'_w \approx 2.5$. In comparison, effects of ε''_w are negligible especially for the lower range of $\varepsilon'_w < 1$. For η, a strictly linear sensitivity is evident that is expected due to Eq. (12). For all three parameters (ε'_w, ε''_w and η), the highest sensitivities are found for Q and U followed by Tb_h and Tb_v. The analysis shown here assists the interpretation and discussion of results presented in Sections 5.2 and 5.3.

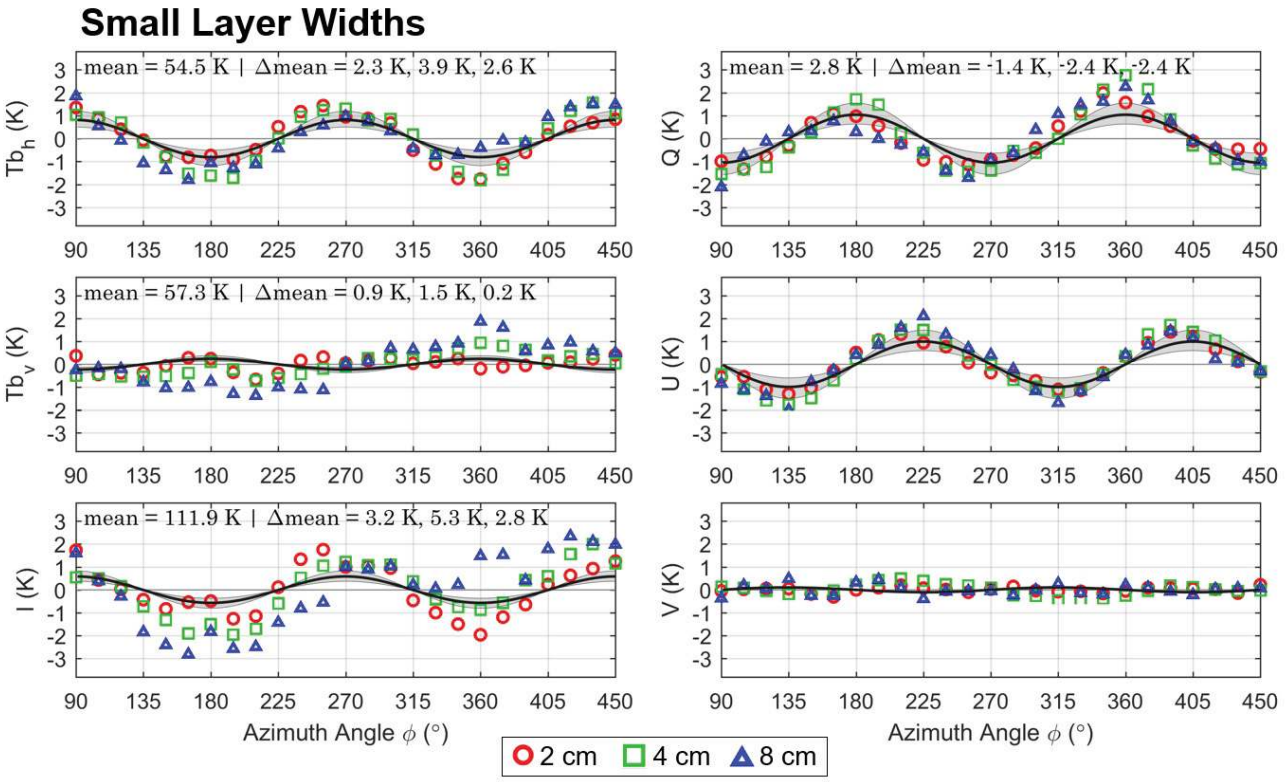

Figure 5. Observed L-band brightness temperature signatures of anisotropic permittivity patterns (2, 4 and 8 cm layer widths) in dependency of the azimuth angle. Solid lines indicate model simulations with parametrization uncertainty bounds (grey shading). All signatures (observations and simulations) have been normalized to zero mean by subtraction of the average brightness temperature level. This level is indicated for simulations (mean) and observations (Δmean = observed mean − simulated mean; same order as legend symbols). Azimuth angles begin at 90° in accordance with the angular convention in Figure 1(b).

5.2. Small Layer Widths

Figure 5 shows brightness temperature observations and model simulations for small permittivity layer widths, here being defined as widths smaller than half the wavelength of observation (2, 4 and 8 cm layers). Model simulations including uncertainty bounds are plotted alongside observations, whereas the lowest (highest) uncertainty bound corresponds to brightness temperature simulations using the lowest (highest) considered values of ε'_w, ε''_w and η (see Table 1).

As general observations, we note that for most polarizations (Tb_h, I, Q and U), brightness temperature measurements show significant azimuthal responses, correspond well with model simulations and show a quasi-equivalent behaviour for all layer widths. These findings suggest that the utilized emission model is valid for up to 8 cm layer widths at L-band. Remaining differences between 2, 4 and 8 cm layer widths are likely at least partly explained by day-to-day variations of the target temperature or background radiance, which are not accounted for in the simulations. Results obtained for the individual polarizations are discussed in the following.

For U and Tb_h, brightness temperature signatures show a clear periodic signature in dependency of the azimuth angle. Both observables show a period of 180° and are phase-shifted by 45° with respect to each other. Brightness temperature observations and simulations are generally in good agreement. Hereby, the observed brightness temperature amplitudes are in many cases on the high end of the simulated confidence bounds ($\sim$ 3–4 K). This could be due to an underestimation of the wood permittivity or target radiance weighing factor (see Section 5.1). For Tb_v, no clear periodic signal was

observed during the experiment. This is likely explained by a combination of factors: Firstly, previous studies indicate that Tb_v observations are particularly sensitive to target imperfections: Similar Tb_v model-observation deviations were found in [32] while simulating the emission of an anisotropic wood material, which was attributed to the imperfect permittivity layering and surface structure of the wood. Secondly, note that model simulations indicate small expected brightness temperature variations (~ 0.4 K) such that uncertainty due to the measurement precision of the instrument (~ 0.1 K for Tb_v) could affect the azimuthal signature. Thirdly, note that observations of 8 cm layers (and to a lesser extent, 4 cm layers) show somewhat periodic brightness temperature variations with a period of 360° (as opposed to the predicted 180° period). This systematic deviation of observed and modelled Tb_v signatures for increasing layer widths could also indicate a gradual polarization-dependent loss of model validity, albeit future studies are needed to confirm this assertion. For V, model simulations indicate only marginal brightness temperature azimuthal variations (amplitudes of ~ 0.2 K). In agreement with this expectation, near-zero levels of V are observed in all cases. Note that a small azimuthal signature is observed for 4 cm layer widths, however, the signature is not in phase with model simulations. This variability could be due to imperfections in the target design.

Signatures of Q and I are functions of Tb_v and Tb_h and can be explained accordingly, as shown in Eq. (1). For Q, a clear azimuthal signature is observed for all permittivity layers which is explained by the periodic behaviour of Tb_h. Signatures of Q are in agreement with model simulations regarding amplitude, period and phase. Remaining differences between Q observations and model simulations (especially with regard to amplitude mismatches) are mostly explained by differences between Tb_v observations and model simulations. For I, a clear azimuthal signature is observed for all permittivity layers, despite observations showing enhanced amplitudes as well as a considerable degree of scattering with respect to model simulations. The latter effect is again explained mainly through differences between Tb_v observations and simulations.

Finally, we note that absolute brightness temperature levels of simulations and observations are generally in good agreement (Δmean not exceeding 2.4 K for Q, Tb_v and 3.9 K for Tb_h). The largest differences are observed for I (2.8–5.3 K), since biases of h- and v-polarized brightness temperatures add up in this case. Among different layer widths, the largest differences occur for 4 cm, which is likely related to the high air temperatures exhibited during the measurements ($\sim$ 23–24°C) leading to highest observed target temperatures (26–27°C) as well as potentially higher background emission contributions. Note again that day-to-day and intra-day variations of the target physical temperature and background radiance are not considered in the simulations (see Sections 4.1 and 4.2). It is expected that biases between simulated and observed brightness temperature levels could be further minimized if variations of these parameters would be considered. In addition, instrument cable and antenna effects can cause constant offsets of up to ~ 1 K for Tb_v and Tb_h that might contribute to the observed biases.

5.3. Large Layer Widths

Figure 6 shows brightness temperature observations and model simulations for large permittivity layer widths, here being defined as widths larger than or approaching the wavelength of observation (16 and 32 cm layers). Note that the emission model is not expected to be valid for these layer widths given an observing wavelength of 21 cm (see Section 2). Despite these limitations, model simulations are plotted alongside observations for comparison purposes, omitting parameter uncertainty bounds for clarity. No comparisons between observed and simulated absolute brightness temperature levels are conducted, noting that such biases are overall low and comparable to the 2, 4 and 8 cm cases (not exceeding 5 K).

For 16 cm layer widths, systematic azimuthal variations are present for Tb_h observations, which follow the amplitude, phase and period of the model signatures. This could be indicative of the model retaining a degree of validity even for permittivity layer widths approaching the wavelength of observation; however, the signatures could also be due to surface structure effects (i.e., the target acting as a periodic surface rather than a uniform material with periodic permittivity). Signatures of Tb_v, U and V show varying degrees of variability in the azimuth direction; however, the observed signatures do not follow the model simulations. Since the model is not expected to be valid at these layer widths, the observed azimuthal variability could be again explained by target imperfections or surface structure effects. Signatures of Q and I show systematic azimuthal variations, which is explained by the systematic variations observed for Tb_h (note again that Q and I are functions of Tb_v and Tb_h, respectively). Hereby,

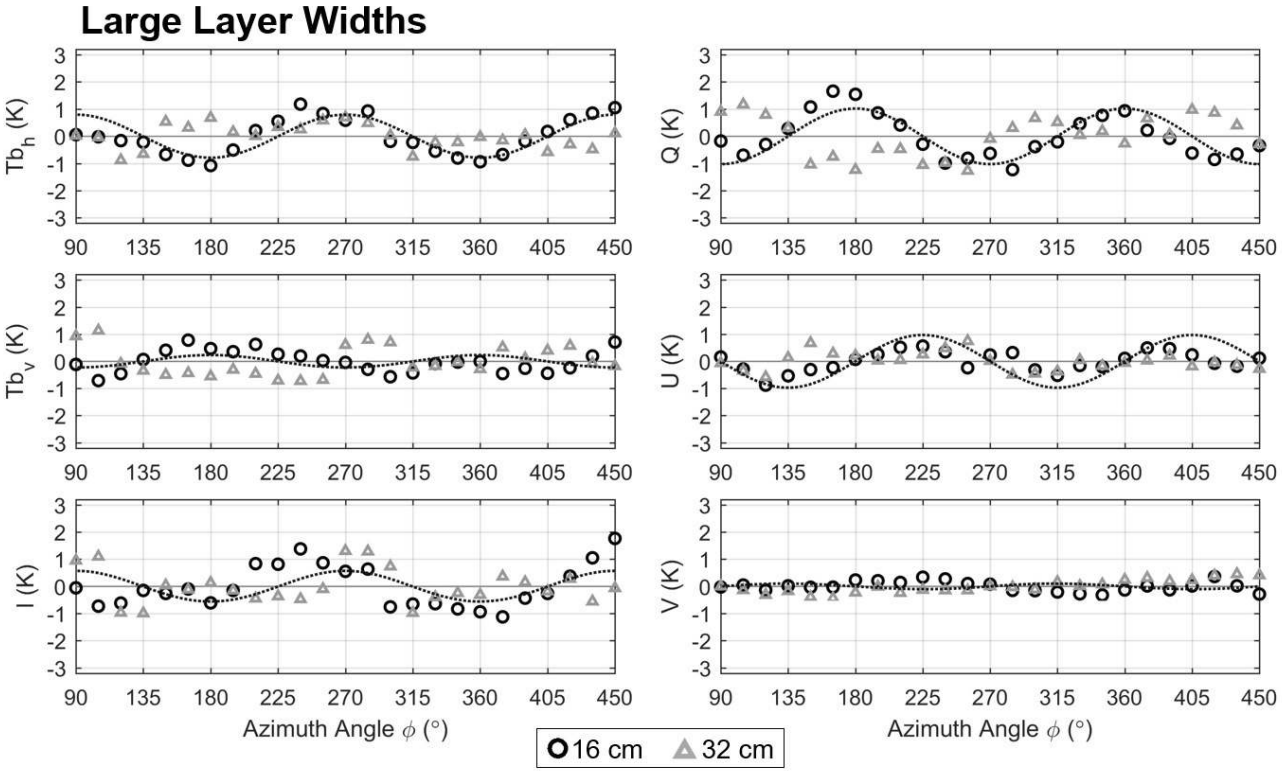

Figure 6. Observed L-band brightness temperature signatures of anisotropic permittivity patterns (16 and 32 cm layer widths) in dependency of the azimuth angle. Model simulations are included in dashed lines for comparison purposes, omitting parameter uncertainty bounds for clarity. All signatures (observations and simulations) have been normalized to zero mean by subtraction of the average brightness temperature level. Azimuth angles begin at 90° in accordance with the angular convention in Figure 1(b).

Q signatures correspond well with model simulations, whereas I signatures show a larger amount of scatter and amplitude mismatch. For both observables, differences between observations and simulations are mainly explained by the influence of Tb_v, which shows a low correspondence to simulations. For 32 cm layer widths, non-systematic azimuthal variations are exhibited for all polarimetric observables, likely due to target imperfections or surface structure effects. Observations do not follow model simulations, confirming the expectation of the model assumptions being violated for layer widths of 32 cm.

6. DISCUSSION

6.1. Field Experiment

The field experiment was designed to (i) assess polarimetric brightness temperature signatures arising from oriented permittivity patterns at L-band and (ii) investigate the maximum permittivity layer widths for which such effects occur. Concerning (i), we note that for practical reasons it was not possible to exactly emulate the model geometry (see Figure 1) by means of the artificial target (see Figure 3). Most notably, while the model assumes an infinite half-space, the utilized target had a finite height of 20 cm. Consequently, transmission effects from the underlying absorber emission are expected to contribute to brightness temperature signatures observed by the radiometer. While such transmission effects were not quantified by means of dedicated measurements during the experiment, the overall good fit between observations and model simulations (considering both absolute signal levels and azimuthal variations) provides indication that such transmission effects had a negligible impact on

Table 2. Estimated permittivity layer width thresholds for X-, C-, L- and P-band.

	Frequency ($\sim$)	Wavelength ($\sim$)	Max. perm. layer width $8\lambda/21$ ($\sim$)
X-band	8–12 GHz	2.5–4 cm	1–1.5 cm
C-band	4–8 GHz	4–7.5 cm	1.5–3 cm
L-band	1–2 GHz	15–30 cm	6–11.5 cm
P-band	250–750 MHz	40–120 cm	15–45 cm

the results at least for the 2, 4 and 8 cm layers. Another difference between model and artificial target is the assumption of uniform permittivity in each layer, which is to some degree violated by the anisotropic permittivity characteristics of wood [45]. However, it is expected that the confidence bounds associated with the wood permittivity parametrization largely compensate for this effect. Note also that the wood planks showed a variety of fiber orientations across the target, ruling out any influence of wood grain on the observed azimuthal effects. Concerning (ii), two points need to be taken into account: Firstly, note that layer widths between 8 and 16 cm were not analysed in this study; consequently, the layer width threshold established here (8 cm) should be strictly interpreted as lower bound. However, since certain model assumptions are expected to be valid only for $d_1, d_2 < \lambda/2$ (i.e., layer widths smaller than $\sim$ 10.5 cm at 1.41 GHz) [32, 35], the threshold established here is expectedly close to the "true" maximum layer width of model validity. Secondly, note that a polarization-dependence of the established layer width threshold could be asserted for few cases (low correspondence between Tb_v observations and simulations for 8 cm layers in Figure 5, good agreement between Tb_h observations and simulations for 16 cm layers in Figure 6). However, since the effects observed in this study are possibly due to a combination of factors (see discussion in Section 5.2), the investigation of this hypothesis is left for future studies.

6.2. Permittivity Patterns in Real-World Scenarios

In this section, the findings of this study are discussed with respect to real-world scenarios, focusing mostly on soil moisture patterns in agricultural settings. Further potential applications exist (e.g., sensing of man-made objects such as laminated/layered structures or natural objects such as wood with distinct fiber orientation [32]) but are not discussed here. We identify three main challenges for transferring the idealized model conditions investigated in this study to real world conditions such as soil moisture patterns:

(i) The maximum permittivity layer width threshold established here is relatively low at L-band (8 cm for 21 cm wavelength). Contrarily, soil moisture patterns were previously observed over row spacings of $\sim$ 50–80 cm [24–30]. Assuming wet and dry soil moisture layers extending to half the row width, this would result in permittivity layer widths of $\sim$ 25–40 cm. For such layer widths and at L-band, no azimuthal brightness temperature variations are expected. However, two points need to be taken into account: Firstly, 18–19 cm row widths are not uncommon for soybean stands [47–49] and have been reported in previous studies for corn stands (although uncommon) [49]. Under extreme conditions such as highly localized irrigation, such row spacings might result in soil moisture patterns of $\sim$ 9–10 cm layer widths. Future studies are needed to confirm the occurrence of soil moisture patterns on such small scales and the transferability of our findings to slightly larger permittivtiy layers ($\sim$ 9–10 cm). Secondly, note that the layer width threshold established here is wavelength-dependent, as is illustrated in Table 2. As a consequence, lower frequency ranges such as P-band are expectedly sensitive to significantly higher permittivity layer widths (up to $\sim$ 15 cm at 750 MHz or $\sim$ 45 cm at 250 MHz), which would be better suited for sensing soil moisture patterns. Conversely, the layer width thresholds are below 3 cm in C- and X-band, rendering these frequency ranges unsuitable for the above purpose.

(ii) The model geometry used in this study is highly idealized. Hereby, at least three points need to be taken into account: Firstly, it remains an open question if an infinite half-space with periodic layers of uniform permittivity is a suitable representation of agricultural soils with moisture patterns. In situ observations and infiltration model simulations indicate that soil moisture patterns tend to show continuous transitions (rather than sharp boundaries) between wet and dry regimes even under

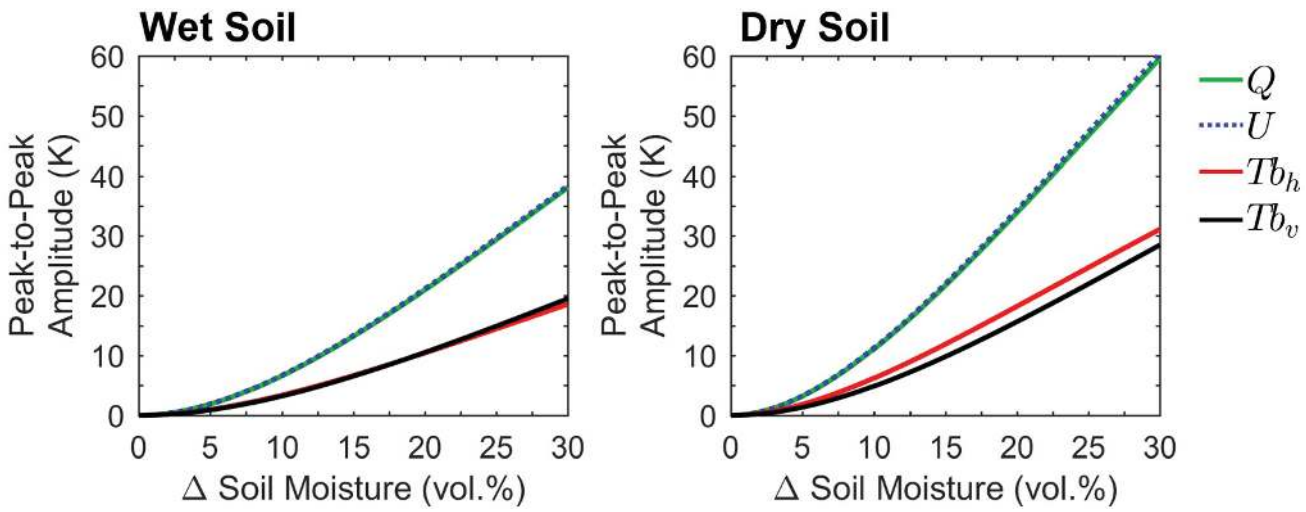

Figure 7. Brightness temperature azimuthal variations resulting from soil moisture patterns under idealized model conditions (see Figure 1). Period and phase of the azimuthal variations are the same as in Figures 5 and 6. Soil moisture differences (Δ Soil Moisture) are expressed with respect to wet soil (20 vol.%) and dry soil (10 vol.%) conditions. All simulations correspond to $\eta = 1$ (see Section 4 for description) and a physical temperature of 293 K. Soil moisture contents were converted to permittivity by means of the model in [51], assuming a clay fraction of 14%.

conditions of localized infiltration from stemflow [28, 29]. However, under extreme conditions such as localized irrigation, high gradients between wet and dry soil regimes have been modelled that could lead to sharp soil permittivity boundaries [28]. Secondly, soil surface roughness plays a significant role for L-band radiometric sensing over agricultural fields [50]. This is true both for small-scale random surface roughness as well as tillage-induced periodic roughness patterns, the latter of which can induce significant azimuth-angle dependent brightness temperature signatures [15]. The emission of soil permittivity patterns under such roughness conditions could differ significantly from the emission observed for a smooth surface, and future investigations are needed to quantify such effects. Thirdly, soil moisture patterns in agricultural fields are often observed as a result of stemflow [28, 29]. In such cases, significant plant cover is expected to be present that could mask azimuth angle dependent brightness temperature signatures from the surface. In addition, plant cover with anisotropic row alignment can itself lead to azimuthal brightness temperature variations [23], which could interfere with azimuthal signatures emitted from the soil.

(iii) Soil moisture patterns are expected to exist only on localized scales, such that the potential relevance for radiometric sensing is expectedly limited to ground-based or airborne studies. In addition, while soil moisture patterns among individual rows have been extensively investigated [24–30], little is known about the spatial persistence of such patterns across rows or even fields. Future research is needed to determine the spatial consistency of row-interrow soil moisture patterns, likely influenced by soil and plant cover heterogeneities as well as localized irrigation practices.

In summary, oriented permittivity patterns are expected to influence L-band brightness temperature signatures only for relatively small layer widths, under conditions that are sufficiently close to an idealized model geometry as well as a sufficiently consistent pattern orientation within the footprint. These constraints expectedly limit L-band radiometric sensing of oriented soil moisture patterns to a small number of hypothetical cases (e.g., patterns of very small row widths due to highly localized irrigation), and future studies are needed to confirm the occurrence of such cases. Soil moisture patterns as reported previously under nominal conditions ($\sim$ 25–40 cm row-interrow width [24–30]) are not expected to induce systematic azimuthal L-band brightness temperature modulations. However, the permittivity layer validity threshold established here ($8\lambda/21$) suggests that lower frequency radiometric observations at P-band are capable of sensing much larger layer widths (up to $\sim$ 45 cm for 250 MHz). While P-band radiometric sensing of soil moisture has been focussed mainly on the

750 MHz range [52, 53], theory suggests relevance of our findings beyond radiometry: Since the scattering amplitudes in Eq. (9) correspond to specular reflection, sensitivity to permittivity patterns is also expected for reflectometry. This could be especially relevant for Signal of Opportunity reflectometry at P-band, where frequencies on the order of ~ 250 MHz can be utilized, comparably high resolutions can be achieved and multiple azimuth angles can be sampled [54–56].

6.3. Expected Signatures from Soil Moisture Patterns under Idealized Conditions

In this section a first investigation on azimuthal brightness temperature variations potentially arising from soil moisture patterns is conducted, keeping in mind the discussion points mentioned in Section 6.2. Figure 7 shows simulated peak-to-peak amplitudes of azimuthal brightness temperature variations resulting from soil moisture patterns under idealized model conditions (see Figure 1). It is evident that soil moisture differences of 8–10 vol.% (which have been observed for both corn and soybean fields [28–30]) would lead to amplitudes of up to ~ 10 K (Q, U) and ~ 4–5 K (Tb_h, Tb_v). Variations are sightly lower when wet soil conditions are assumed, since soil moisture differences lead to higher relative permittivity gradients for dry soils. For an extreme hypothetical case of 30 vol.% difference, which was modelled in [28] as a result of localized irrigation, amplitudes reach even higher values (~ 60 K for Q and U). Note that these simulations correspond to the case of $\eta = 1$, which largely explains the significantly higher amplitudes in Figure 7 with respect to Figures 5 and 6. Note also that while the results in Figure 7 are for L-band, only slightly higher amplitudes would result for P-band (less than 8% difference for 250 MHz with respect to 1.4 GHz, not shown). In summary, despite the simulations in Figure 7 correspond to a highly idealized model geometry (and thus remain of hypothetical nature), they illustrate the potential impact of permittivity patterns resulting from realistic soil moisture differences on polarimetric brightness temperature observations.

7. CONCLUSIONS

This study has shown that oriented permittivity patterns of up to 8 cm layer widths lead to systematic L-band brightness temperature modulations in dependency of the azimuthal look angle. For the artificial target used here, modulations reach amplitudes of ~ 4 K (Tb_h, I, Q and U polarizations), whereas simulations of soil moisture patterns under idealized conditions indicate even higher amplitudes (up to 60 K for extreme cases). However, due to the relatively small permittivity layer widths observable at L-band (8 cm given a wavelength of 21 cm), soil moisture patterns under nominal conditions (~ 25–40 cm row-interrow width [24–30]) are not expected to induce systematic L-band brightness temperature modulations. In addition, it remains an open question whether the idealized model geometry assessed here is suitable to represent permittivity conditions in agricultural soils even when extreme cases such as localized irrigation are assumed. Consequently, future studies are needed to transfer the findings to potential remote sensing applications, which, in addition to soil moisture patterns, could include the sensing of man-made objects (e.g., laminated/layered structures) or natural materials with anisotropic permittivity (e.g., fiber orientation of wood). The permittivity layer threshold estimated here experimentally (8/21 wavelengths) provides guidance on the selection of suitable frequency ranges: For the soil moisture case, P-band radiometry [52, 53] and reflectometry [54–56] might be of particular interest, since significantly larger permittivity layers (up to ~ 45 cm) can expectedly be observed.

ACKNOWLEDGMENT

The authors thank M. Soellner for providing the code of the microwave emission model utilized in this study and S. Thurner (DLR) for conducting the Styrofoam permittivity measurements. We gratefully acknowledge the support of TERENO (Terrestrial Environmental Observatories) funded by the Helmholtz-Gemeinschaft. This research was partly funded by the German Research Foundation (DFG), grant number JO 1262/2-1.

APPENDIX A.

The transformation matrix $\underline{M}$ of Eq. (8) is given by [32]:

$$\underline{M} = \begin{bmatrix} \sin\phi & \cos\theta\cos\phi & 0 & \alpha_x \sin\theta\cos\phi \\ -\cos\phi & \cos\theta\sin\phi & a \cdot k'_{zo} & \alpha_y \sin\theta\sin\phi \\ \cos\theta\cos\phi & -\sin\phi & a \cdot \left(\varepsilon_y - \sin^2\theta\cos^2\phi\right) & 0 \\ \cos\theta\sin\phi & \cos\phi & -a \cdot \sin^2\theta\cos\phi\sin\phi & (\alpha_y - \alpha_x) \cdot \sin\theta\cos\phi \cdot k'_{zeo} \end{bmatrix}, \tag{A1}$$

with

$$\begin{aligned} a &= \frac{1}{\sqrt{n_o^2 - \sin^2\theta \cdot \cos^2\phi}}, \\ k'_{zeo} &= \sqrt{n_{eo}^2 - \sin^2\theta}, \\ k'_{zo} &= \sqrt{n_o^2 - \sin^2\theta}. \end{aligned} \tag{A2}$$

APPENDIX B.

The scattering amplitudes f_{hh}, f_{hv}, f_{vh} and f_{vv} of Eq. (9) are given by [32]:

$$\begin{aligned} f_{hh} &= \frac{1}{f} \cdot \left[a_{22v}\left(a_{11h} - a_{12h}\right) - \left(a_{11v} + a_{12v}\right) \cdot \left(a_{21h} - a_{22h}\right)\right], \\ f_{hv} &= \frac{2}{f} \cdot \left[a_{22v} \cdot a_{11v}\right], \\ f_{vh} &= \frac{2}{f} \cdot \left[a_{12h} \cdot a_{21h} - a_{11h} \cdot a_{22h}\right], \\ f_{vv} &= \frac{1}{f} \cdot \left[-a_{22v}\left(a_{11h} + a_{12h}\right) - \left(a_{11v} - a_{12v}\right) \cdot \left(a_{21h} + a_{22h}\right)\right], \\ f &= a_{22v}\left(a_{11h} + a_{12h}\right) - \left(a_{21h} + a_{22h}\right) \cdot \left(a_{11v} + a_{12v}\right), \end{aligned} \tag{B1}$$

with

$$\begin{aligned} a_{11h} &= k'_{zo} \cdot \alpha_x \cos\theta \cdot \cos^2\phi, \\ a_{12h} &= \left(\alpha_y \sin^2\phi + \alpha_x \cos^2\phi\right) \cdot \left(\varepsilon_y - \sin^2\theta \cdot \cos^2\phi\right), \\ a_{11v} &= \cos\theta \cdot \sin\phi \cdot \cos\phi \cdot (\alpha_y - \alpha_x) \cdot \left(\varepsilon_y - \sin^2\theta \cdot \cos^2\phi\right), \\ a_{12v} &= -k'_{zo} \cdot \alpha_x \sin\phi \cdot \cos\phi, \\ a_{21h} &= \cos\theta \cdot \left(\varepsilon_y \sin^2\phi + k'_{zeo} \cdot k'_{zo} \cos^2\phi\right), \\ a_{22h} &= k'_{zeo} \cdot \left(\varepsilon_y - \sin^2\theta \cdot \cos^2\phi\right), \\ a_{22v} &= \sin\phi \cdot \cos\phi \cdot k'_{zo} \cdot \left(k'_{zo} - k'_{zeo}\right). \end{aligned} \tag{B2}$$

REFERENCES

1. Njoku, E. G. and D. Entekhabi, "Passive microwave remote sensing of soil moisture," *Journal of Hydrology*, Vol. 184, Nos. 1–2, 101–129, 1996.
2. Babaeian, E., M. Sadeghi, S. B. Jones, C. Montzka, H. Vereecken, and M. Tuller, "Ground, proximal, and satellite remote sensing of soil moisture," *Reviews of Geophysics*, Vol. 57, No. 2, 530–616, 2019.
3. Kerr, Y. H., P. Waldteufel, J.-P. Wigneron, S. Delwart, F. Cabot, J. Boutin, M.-J. Escorihuela, J. Font, N. Reul, C. Gruhier, et al., "The SMOS mission: New tool for monitoring key elements ofthe global water cycle," *Proceedings of the IEEE*, Vol. 98, No. 5, 666–687, 2010.

4. Entekhabi, D., E. G. Njoku, P. E. O'Neill, K. H. Kellogg, W. T. Crow, W. N. Edelstein, J. K. Entin, S. D. Goodman, T. J. Jackson, J. Johnson, et al., "The soil moisture active passive (SMAP) mission," *Proceedings of the IEEE*, Vol. 98, No. 5, 704–716, 2010.
5. Font, J., A. Camps, A. Borges, M. Martín-Neira, J. Boutin, N. Reul, Y. H. Kerr, A. Hahne, and S. Mecklenburg, "SMOS: The challenging sea surface salinity measurement from space," *Proceedings of the IEEE*, Vol. 98, No. 5, 649–665, 2009.
6. Roy, A., A. Royer, C. Derksen, L. Brucker, A. Langlois, A. Mialon, and Y. H. Kerr, "Evaluation of spaceborne L-band radiometer measurements for terrestrial freeze/thaw retrievals in Canada," *IEEE Journal of Selected Topics in Applied Earth Observations and Remote Sensing*, Vol. 8, No. 9, 4442–4459, 2015.
7. Mills, P. and G. Heygster, "Retrieving ice concentration from SMOS," *IEEE Geoscience and Remote Sensing Letters*, Vol. 8, No. 2, 283–287, 2010.
8. Rautiainen, K., T. Parkkinen, J. Lemmetyinen, M. Schwank, A. Wiesmann, J. Ikonen, C. Derksen, S. Davydov, A. Davydova, J. Boike, et al., "SMOS prototype algorithm for detecting autumn soil freezing," *Remote Sensing of Environment*, Vol. 180, 346–360, 2016.
9. Kaleschke, L., X. Tian-Kunze, N. Maaß, M. Mäkynen, and M. Drusch, "Sea ice thickness retrieval from SMOS brightness temperatures during the Arctic freeze-up period," *Geophysical Research Letters*, Vol. 39, No. 5, 2012.
10. Randa, J., J. Lahtinen, A. Camps, A. Gasiewski, M. Hallikainen, D. M. Le Vine, M. Martin-Neira, J. Piepmeier, P. W. Rosenkranz, C. S. Ruf, et al., "Recommended terminology for microwave radiometry," NIST Technical Note TN1551, Vol. 27, 2008.
11. Tsang, L., "Polarimetic passive microwave remote sensing of random discrete scatterers and rough surfaces," *Journal of Electromagnetic Waves and Applications*, Vol. 5, No. 1, 41–57, 1991.
12. Tsang, L., "Thermal emission of nonspherical particles," *Radio Science*, Vol. 19, No. 4, 966–974, 1984.
13. Yueh, S. H., W. J. Wilson, S. J. Dinardo, and F. K. Li, "Polarimetric microwave brightness signatures of ocean wind directions," *IEEE Transactions on Geoscience and Remote Sensing*, Vol. 37, No. 2, 949–959, 1999.
14. Veysoglu, M. E., H. Yueh, R. Shin, and J. Kong, "Polarimetric passive remote sensing of periodic surfaces," *Journal of Electromagnetic Waves and Applications*, Vol. 5, No. 3, 267–280, 1991.
15. Sobjaerg, S. and N. Skou, "Polarimetric signatures from a crop covered land surface measured by an L-band polarimetric radiometer," *2003 IEEE International Geoscience and Remote Sensing Symposium, IGARSS 2003, Proceedings (IEEE Cat. No. 03CH37477)*, Vol. 4, 2626–2628, IEEE, 2003.
16. Hornbuckle, B. K., A. W. England, R. D. De Roo, M. A. Fischman, and D. L. Boprie, "Vegetation canopy anisotropy at 1.4 GHz," *IEEE Transactions on Geoscience and Remote Sensing*, Vol. 41, No. 10, 2211–2223, 2003.
17. O'Neill, P., T. Jackson, B. Blanchard, J. Wang, and W. Gould, "Effects of corn stalk orientation and water content on passive microwave sensing of soil moisture," *Remote Sensing of Environment*, Vol. 16, No. 1, 55–67, 1984.
18. Brunfeldt, D. R. and F. T. Ulaby, "Microwave emission from row crops," *IEEE Transactions on Geoscience and Remote Sensing*, Vol. 24, No. 3, 353–359, 1986.
19. Colliander, A., S.-B. Kim, S. H. Yueh, M. H. Cosh, T. J. Jackson, and E. G. Njoku, "Azimuthal signature of coincidental brightness temperature and normalized radar cross-section obtained using airborne PALS instrument," *PIERS Online*, Vol. 6, No. 6, 500–503, 2010.
20. Narvekar, P. S., T. J. Jackson, R. Bindlish, L. Li, G. Heygster, and P. Gaiser, "Observations of land surface passive polarimetry with the WindSat instrument," *IEEE Transactions on Geoscience and Remote Sensing*, Vol. 45, No. 7, 2019–2028, 2007.
21. Wang, J. R., R. W. Newton, and J. W. Rouse, "Passive microwave remote sensing of soil moisture: The effect of tilled row structure," *IEEE Transactions on Geoscience and Remote Sensing*, No. 4, 296–302, 1980.

22. Promes, P., T. Jackson, and P. O'Neill, "Significance of agricultural row structure on the microwave emissivity of soils," *IEEE Transactions on Geoscience and Remote Sensing*, Vol. 26, No. 5, 580–589, 1988.
23. Macelloni, G., P. Pampaloni, S. Paloscia, and R. Ruisi, "Effects of spatial inhomogeneities and microwave emission enhancement in random media: An experimental study," *IEEE Transactions on Geoscience and Remote Sensing*, Vol. 34, No. 5, 1084–1089, 1996.
24. Van Wesenbeeck, I. and R. Kachanoski, "Spatial and temporal distribution of soil water in the tilled layer under a corn crop," *Soil Science Society of America Journal*, Vol. 52, No. 2, 363–368, 1988.
25. Zhai, R., R. Kachanoski, and R. Voroney, "Tillage effects on the spatial and temporal variations of soil water," *Soil Science Society of America Journal*, Vol. 54, No. 1, 186–192, 1990.
26. Paltineanu, I. and J. Starr, "Preferential water flow through corn canopy and soil water dynamics across rows," *Soil Science Society of America Journal*, Vol. 64, No. 1, 44–54, 2000.
27. Starr, J. L. and D. J. Timlin, "Using high-resolution soil moisture data to assess soil water dynamics in the vadose zone," *Vadose Zone Journal*, Vol. 3, No. 3, 926–935, 2004.
28. Martello, M., N. Ferro, L. Bortolini, and F. Morari, "Effect of incident rainfall redistribution by maize canopy on soil moisture at the crop row scale," *Water*, Vol. 7, No. 5, 2254–2271, 2015.
29. Canone, D., M. Previati, and S. Ferraris, "Evaluation of stem flow effects on the spatial distribution of soil moisture using TDR monitoring and an infiltration model," *Journal of Irrigation and Drainage Engineering*, Vol. 143, No. 1, 04016075, 2016.
30. Timlin, D., Y. Pachepsky, and V. R. Reddy, "Soil water dynamics in row and interrow positions in soybean (Glycine max L.)," *Plant and Soil*, Vol. 237, No. 1, 25–35, 2001.
31. Prieksat, M., T. Kaspar, and M. Ankeny, "Positional and temporal changes in ponded infiltration in a corn field," *Soil Science Society of America Journal*, Vol. 58, No. 1, 181–184, 1994.
32. Sollner, M., "Vollpolarimetrische Helligkeitstemperatur-Verteilungen von natürlichen und künstlichen Objekten bei einer Frequenz von 90 GHz," DLR Research Report 98-19, DLR Library and Information Center, Cologne, ISSN 1434-8454, 1998.
33. Rytov, S., "Electromagnetic properties of a finely stratified medium," *Soviet Physics JEPT*, Vol. 2, 466–475, 1956.
34. Born, M. and E. Wolf, *Principles of Optics: Electromagnetic Theory of Propagation, Interference and Diffraction of Light*, Elsevier, 2013.
35. Lorente-Crespo, M., G. Ballesteros, and C. Mateo-Segura, "All-dielectric broadband microwave polarization conversion based on form birefringence," *2015 9th International Congress on Advanced Electromagnetic Materials in Microwaves and Optics (Metamaterials)*, 184–186, IEEE, 2015.
36. Jonard, F., L. Weihermüller, M. Schwank, K. Z. Jadoon, H. Vereecken, and S. Lambot, "Estimation of hydraulic properties of a sandy soil using ground-based active and passive microwave remote sensing," *IEEE Transactions on Geoscience and Remote Sensing*, Vol. 53, No. 6, 3095–3109, 2015.
37. Søbjærg, S. S., S. S. Kristensen, J. E. Balling, and N. Skou, "The airborne EMIRAD L-band radiometer system," *2013 IEEE International Geoscience and Remote Sensing Symposium — IGARSS*, 1900–1903, IEEE, 2013.
38. Jonard, F., S. Bircher, F. Demontoux, L. Weihermüller, S. Razandratsima, J.-P. Wigneron, and H. Vereecken, "Passive L-band microwave remote sensing of organic soil surface layers: A tower-based experiment," *Remote Sensing*, Vol. 10, No. 2, 304, 2018.
39. Søbjærg, S. S., J. E. Balling, and N. Skou, "Performance assessment of an LNA used as active cold load," *2015 IEEE International Geoscience and Remote Sensing Symposium (IGARSS)*, 4742–4745, IEEE, 2015.
40. Baker-Jarvis, J., E. J. Vanzura, and W. A. Kissick, "Improved technique for determining complex permittivity with the transmission/reflection method," *IEEE Transactions on Microwave Theory and Techniques*, Vol. 38, No. 8, 1096–1103, 1990.
41. Glass, S. V. and S. L. Zelinka, "Moisture relations and physical properties of wood," *Wood Handbook: Wood as an Engineering Material*, Centennial ed., Chapter 4, Vol. 190, 4–1, General

technical report FPL; GTR-190, Madison, WI: US Dept. of Agriculture, Forest Service, Forest Products Laboratory, 2010.

42. Ahmet, K., G. Dai, R. Tomlin, P. Kaczmar, and S. Riddiough, "The equilibrium moisture content of common UK species at three conditions of temperature and relative humidity," *Forest Products Journal*, Vol. 50, No. 6, 2000.
43. Razafindratsima, S., Z. M. Sbartaï, and F. Demontoux, "Permittivity measurement of wood material over a wide range of moisture content," *Wood Science and Technology*, Vol. 51, No. 6, 1421–1431, 2017.
44. Mai, T. C., S. Razafindratsima, Z. M. Sbartaï, F. Demontoux, and F. Bos, "Non-destructive evaluation of moisture content of wood material at GPR frequency," *Construction and Building Materials*, Vol. 77, 213–217, 2015.
45. Sahin, H. and N. Ay, "Dielectric properties of hardwood species at microwave frequencies," *Journal of Wood Science*, Vol. 50, No. 4, 375–380, 2004.
46. Cox, W. J. and D. J. Cherney, "Row spacing, plant density, and nitrogen effects on corn silage," *Agronomy Journal*, Vol. 93, No. 3, 597–602, 2001.
47. Zhou, X., G. Yang, S. Sun, and Y. Chen, "Plant and row spacing effects on soil water and yield of rainfed summer soybean in the northern China," *Plant, Soil and Environment*, Vol. 56, No. 1, 1–7, 2012.
48. Frederick, J. R., P. J. Bauer, W. J. Busscher, and G. S. McCutcheon, "Tillage management for doublecropped soybean grown in narrow and wide row width culture," *Crop Science*, Vol. 38, No. 3, 755–762, 1998.
49. Pedersen, P. and J. G. Lauer, "Corn and soybean response to rotation sequence, row spacing, and tillage system," *Agronomy Journal*, Vol. 95, No. 4, 965–971, 2003.
50. Wigneron, J.-P., L. Laguerre, and Y. H. Kerr, "A simple parameterization of the L-band microwave emission from rough agricultural soils," *IEEE Transactions on Geoscience and Remote Sensing*, Vol. 39, No. 8, 1697–1707, 2001.
51. Mironov, V. L., L. G. Kosolapova, and S. V. Fomin, "Physically and mineralogically based spectroscopic dielectric model for moist soils," *IEEE Transactions on Geoscience and Remote Sensing*, Vol. 47, No. 7, 2059–2070, 2009.
52. Ye, N., X. Wu, J. Walker, N. Boopathi, T. J. Jackson, Y. Kerr, E. Kim, A. McGrath, I.-Y. Yeo, and M. Moghaddam, "Towards multi-frequency soil moisture retrieval using P- and L-band passive microwave sensing technology," *IGARSS 2018 — 2018 IEEE International Geoscience and Remote Sensing Symposium*, 3707–3710, IEEE, 2018.
53. Boopathi, N., N. Ye, X. Wu, J. P. Walker, Y. Rao, T. J. Jackson, Y. Kerr, E. Kim, A. McGrath, and I.-Y. Yeo, "Towards soil moisture retrieval using tower-based p-band radiometer observations," *IGARSS 2018 — 2018 IEEE International Geoscience and Remote Sensing Symposium*, 1407–1410, IEEE, 2018.
54. Yueh, S. H., X. Xu, R. Shah, S. Margulis, and K. Elder, "P-band signals of opportunity for remote sensing of root zone soil moisture," *IGARSS 2018 — 2018 IEEE International Geoscience and Remote Sensing Symposium*, 1403–1406, IEEE, 2018.
55. Knuble, J., J. Piepmeier, M. Deshpande, C. Du Toit, J. Garrison, Y.-C. Lin, G. Stienne, S. Katzberg, and G. Alikakos, "Airborne P-band Signal of Opportunity (SoOP) demonstrator instrument; status update," *2016 IEEE International Geoscience and Remote Sensing Symposium (IGARSS)*, 5638–5641, IEEE, 2016.
56. Yueh, S., R. Shah, X. Xu, K. Elder, and B. Starr, "Experimental demonstration of soil moisture remote sensing using P-band satellite signals of opportunity," *IEEE Geoscience and Remote Sensing Letters*, 1–5, IEEE, 2019.